Effects of Fibre Orientation on Electrocardiographic and Mechanical Functions in a Computational Human Biventricular Model

Lei Wang[1](✉), Zhinuo J. Wang[1], Ruben Doste[1], Alfonso Santiago[2], Xin Zhou[1], Adria Quintanas[2], Mariano Vazquez[2], and Blanca Rodriguez[1]

[1] Department of Computer Science, University of Oxford, Oxford, UK
lei.wang@cs.ox.ac.uk
[2] Barcelona Supercomputing Centre (BSC), Barcelona, Spain

Abstract. The helix orientated fibres in the ventricular wall modulate the cardiac electromechanical functions. Experimental data of the helix angle through the ventricular wall have been reported from histological and image-based methods, exhibiting large variability. It is, however, still unclear how this variability influences electrocardiographic characteristics and mechanical functions of human hearts, as characterized through computer simulations. This paper investigates the effects of the range and transmural gradient of the helix angle on electrocardiogram, pressure-volume loops, circumferential contraction, wall thickening, longitudinal shortening and twist, by using state-of-the-art computational human biventricular modelling and simulation. Five models of the helix angle are considered based on *in vivo* diffusion tensor magnetic resonance imaging data. We found that both electrocardiographic and mechanical biomarkers are influenced by these two factors, through the mechanism of regulating the proportion of circumferentially-orientated fibres. With the increase in this proportion, the T-wave amplitude decreases, circumferential contraction and twist increase while longitudinal shortening decreases.

Keywords: Fibre orientation · Electromechanical modelling and simulation · Helix angle range · ECG · Pressure volume loops

1 Introduction

The heart is an electrically-driven pump that pushes blood to circulate through the body and lungs by periodic contraction and relaxation of the myocardium. The electromechanical function of the cardiac ventricles depends on the underlying microstructure of myocyte aggregation [1]. Based on histological analysis, the myocardium has been structurally modelled as a helix aggregation of the rod-shaped myocyte within extracellular matrix [2], with anisotropy in the electric propagation, active tension generation and resistance to passive deformation [3]. Light-microscopy has also shown the helical

© Springer Nature Switzerland AG 2021
D. B. Ennis et al. (Eds.): FIMH 2021, LNCS 12738, pp. 351–361, 2021.
https://doi.org/10.1007/978-3-030-78710-3_34

structure in the canine heart [4], and the transmural variation in the helix angle has been commonly reported in many species, including porcine [5] and human [6].

The *helix angle* is commonly defined as the angle between fibre orientation and the ventricular circumferential direction. The reported range of helix angle from *in vivo* diffusion tensor magnetic resonance imaging (DTMRI) of the human ventricles varies from study to study: 30°~−40° [7], 55°~−30° [8], 60°~−60° [9] and 90°~−90° [10]. The range from DTMRI data was found lower than that from the histological data (see Fig. 3 in [11]). Some possible reasons for this are the different heart states and a noisy DTMRI signal at the endocardium and epicardium [11], which are just the locations for measuring the range of helix angle.

The transmural gradient of the helix angle also varies from linear to nonlinear. A nonlinear transmural variation of 90°~−80° from the endocardium to the epicardium (see Fig. 4 in [4]) was reported from the histological analysis of a canine heart. The proportion of cir*cumferentially* (0 ± 22.5°) to *longitudinally orientated fibres* (±67.5 to ±90°) is approximately 10:1 [4]. A similar nonlinearity is observed in the histological analysis of a human heart with a smaller transmural range of helix angles, about 50°~−80° (see Fig. 16 in [6]). The transmural gradient of helix angle has been found to influence contraction [12] and diastolic filling [13] through computation models of rat left ventricle. It is however still unclear how the transmural gradient of the helix angle modulates the electromechanical function of human ventricles.

This paper investigates the effects of fibre orientation on clinical electrocardiographic and mechanical biomarkers using high-performance computer (HPC) simulations with a multiscale model of the human biventricular electromechanical function. Specifically, we evaluate the roles of range and transmural gradient of the helix angle on the simulated electrocardiogram (ECG), pressure-volume (PV) loops, left ventricular ejection fraction (LVEF), circumferential contraction, wall thickening, longitudinal shortening and twist. Unravelling the impact of fibre orientation on clinical markers through computational modelling and simulation is important to aid in data interpretation, and facilitate advancements in image acquisition and analysis to characterise human ventricular fibre architecture.

2 Method

2.1 Image-Based Human Biventricular Multiscale Model of Healthy Electromechanical Function

The human image-based biventricular electromechanical modelling and simulation framework developed, calibrated and evaluated in [14] was used as the basis of this study, see Fig. 1. Briefly, electrical propagation was simulated using the monodomain equation with the latest ToR-ORd model [15] for the human-based cellular membrane kinetics. The myocyte active contractile force generation was modelled using the human-based active tension of Land *et al.* model [16], coupled to the ToR-ORd as in [17]. The passive mechanics was based on the Holzapfel-Ogden model [18].

The human ventricular electromechanical model was implemented as a strongly-coupled system in the HPC numerical software, Alya [19], and simulations were conducted in the supercomputer Piz Daint in the Swiss National Supercomputing Centre.

The simulation per heartbeat, for a mesh with over 1.1 M linear tetrahedral elements, takes about 1.7 h on 10 nodes. The physiological conduction velocities of 67 cm/s, 30 cm/s, and 17 cm/s along the fibre, sheet, and sheet-normal directions were achieved by calibrating the diffusivities for this mesh in [14]. The same mesh was used throughout the study for different cases with variations of fibre orientations, and the mesh resolution should have little effects on the results since the conduction velocity has been calibrated.

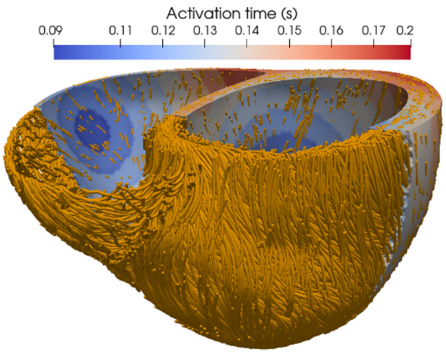

Geometry at diastasis	
LV-volume	103.3 mL
RV-volume	89.7 mL
Boundary conditions	
Endocardium	Pressure determined by two-element Windkessel flow model
Epicardium	Constrained by the elastic spring
Base	Fixed
Stimulus	
The current of 0.2 mA is applied at seven root patches for 1ms per 1 second.	

Fig. 1. Geometry of the human biventricular model with fibre structure and activation time map. Mechanical boundary conditions are applied to the endocardium, epicardium and base for a realistic deformation. Electrical propagation is elicited by stimulation on the entire endocardial surface originating from seven root nodes, as in [14], to mimic Purkinje-like activation.

2.2 Five Models of Helix Angle Variation

To evaluate the role of variability in fibre orientation in modulating ventricular electrocardiographic and mechanical biomarkers, five models of the helix angle in Table 1 were incorporated into the human biventricular model described in [14].

In Cases 1–4, the helix angle range varies based on the report in [7–10], with an assumed linear transmural gradient. However, with this linear variation, the histogram of the helix angle is inconsistent with that from the measurement in [10], which is a bell-shaped curve (see Fig. 3 in [10]). Instead, a nonlinear variation can produce this histogram, see Fig. 2 for Cases 4 and 5. Comparison of results from Case 5 to 4 can show the effects of nonlinear transmural gradient in the helix angle.

2.3 Quantification of Clinical Electrocardiographic and Mechanical Biomarkers

The simulated ECGs were computed by Alya on the fly using the pseudo-ECG method (spatial integral of the gradient of membrane potentials) at each time step [20, 21]. The electrocardiographic biomarkers, QRS duration, QT interval, T-wave amplitude, were quantified from the simulated ECGs. The start time of Q-wave and end times of S-, T-waves were identified through changes in the gradient of ECG signal.

The mechanical biomarkers, end-diastolic volume (EDV), end-systolic volume (ESV), ejection fraction (EF), ejection pressure, were quantified from the computed

Table 1. Five models of helix angle variation considered in the study, parameterized by the helix angle (α) range from endocardium to epicardium (second column), their transmural gradient through the left ventricular wall (as linear or nonlinear, third and fourth column), and proportion of circumferentially-oriented fibres with helix angle between ±22.5° across the myocardium (fifth column). Variable t indicates a transmural position in the wall, and it is the percent of the distance between the position and endocardium out of the wall thickness.

Case no.	Helix angle range: endo ($t = 0$) ~ epi ($t = 100$)	Transmural gradient	Helix angles, α (°) $0 < t < 100$	Proportion of fibres with $-22.5° < \alpha < 22.5°$
1	30°~−40° [7]	Linear	$-0.7t + 30$	64%
2	55°~−30° [8]	Linear	$-0.85t + 55$	53%
3	60°~−60° [9]	Linear	$-1.2(t - 50)$	37%
4	90°~−90° [10]	Linear	$-1.8(t - 50)$	25%
5	90°~−90° [10]	Nonlinear	$-0.0005(t - 50)^3$ $-0.658(t - 50)$	48%

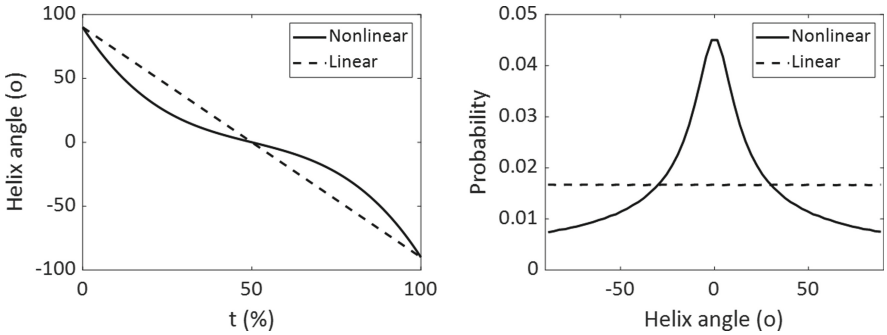

Fig. 2. Left: the helix angle through the left ventricular wall in Case 4 (linear transmural gradient) and Case 5 (nonlinear transmural gradient). Right: Histogram of helix angle values in Case 4 and Case 5, in which the histogram of the nonlinear model is consistent with that from the *in vivo* measurement of the human heart in [10].

PV loops. In each time step, the mean of each normal strain component in the circumferential-transmural-longitudinal coordinate system over all mesh nodes was computed as

$$mean\ E_{xx} = \frac{\sum_{i=1}^{N} E_{xx}^{(i)}}{N},$$

where, $xx = \{cc, tt, ll\}$ indicates the circumferential, transmural and longitudinal normal strain components, N is the number of mesh nodes, and $E_{xx}^{(i)}$ is the normal strain component of the node with index i along x direction. For any node on the endocardium, the transmural direction was determined by the vector to the node on the epicardium such

that their distance is the shortest. The longitudinal direction was parallel to the apex-base direction, and the circumferential direction was orthogonal to both transmural and longitudinal directions. The circumferential contraction was *indicated* by the mean of circumferential strain, the longitudinal shortening by the mean of longitudinal strain, and the wall thickening by the mean of transmural strain, as they are naturally correlated. For example, when comparing results between different cases, a larger circumferential strain indicates larger circumferential expansion, and a lower circumferential strain or larger negative circumferential strain indicates larger circumferential contraction.

The twist angle is the relative rotational angle of the apex to the base. As shown in Fig. 3, the rotational angle of the apex was quantified by selecting all of the mesh nodes of the LV wall in a slice near the apex and parallel to the basal plane, and the average of the rotational angles over the selected nodes was computed and reported for each time step. Since the basal plane was fixed in our computation model [14], the twist angle was equal to this averaged rotational angle.

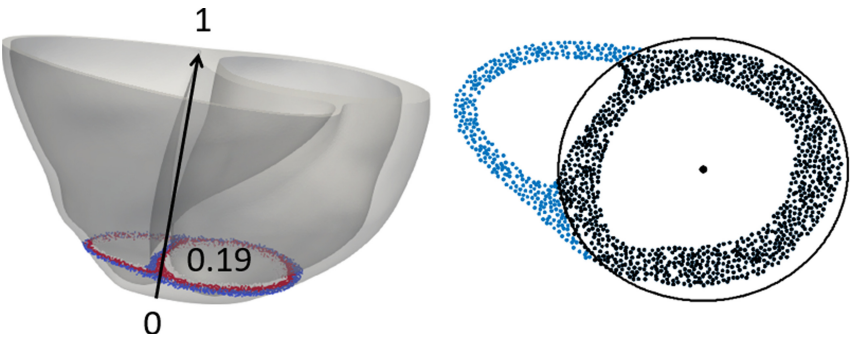

Fig. 3. Twist angle was computed by selecting a slice close to the apex (19% of the apex-base distance) parallel to the basal plane (left), and computing the rotational angles on the black-coloured nodes in the LV wall for each time step (right).

3 Results

The variation of electrocardiographic and mechanical biomarkers with altering the range and the helix angle transmural gradient were extracted from simulation results for the Cases 1–5 described in Table 1.

The comparison of mechanical effects between Cases 1–4 with various helix angle ranges is shown in Fig. 4(a)–(c). The PV loops show that the ejection pressure increases from Case 1 to 4, with increase in helix angle range, indicating a positive correlation between the ejection pressure and helix angle range. The LVESV in Case 3 is smaller than in other cases, so with a similar LVEDV for Cases 1–4, the LVEF in Case 3 is larger than in other cases. This is due to an intermediate helix angle range in Case 3 and a more detailed discussion on this point is provided in the next section.

Figure 4(d)–(g) shows effects of the helix angle range on simulated mean of circumferential, transmural and longitudinal strain, and twist angle of the apex against time.

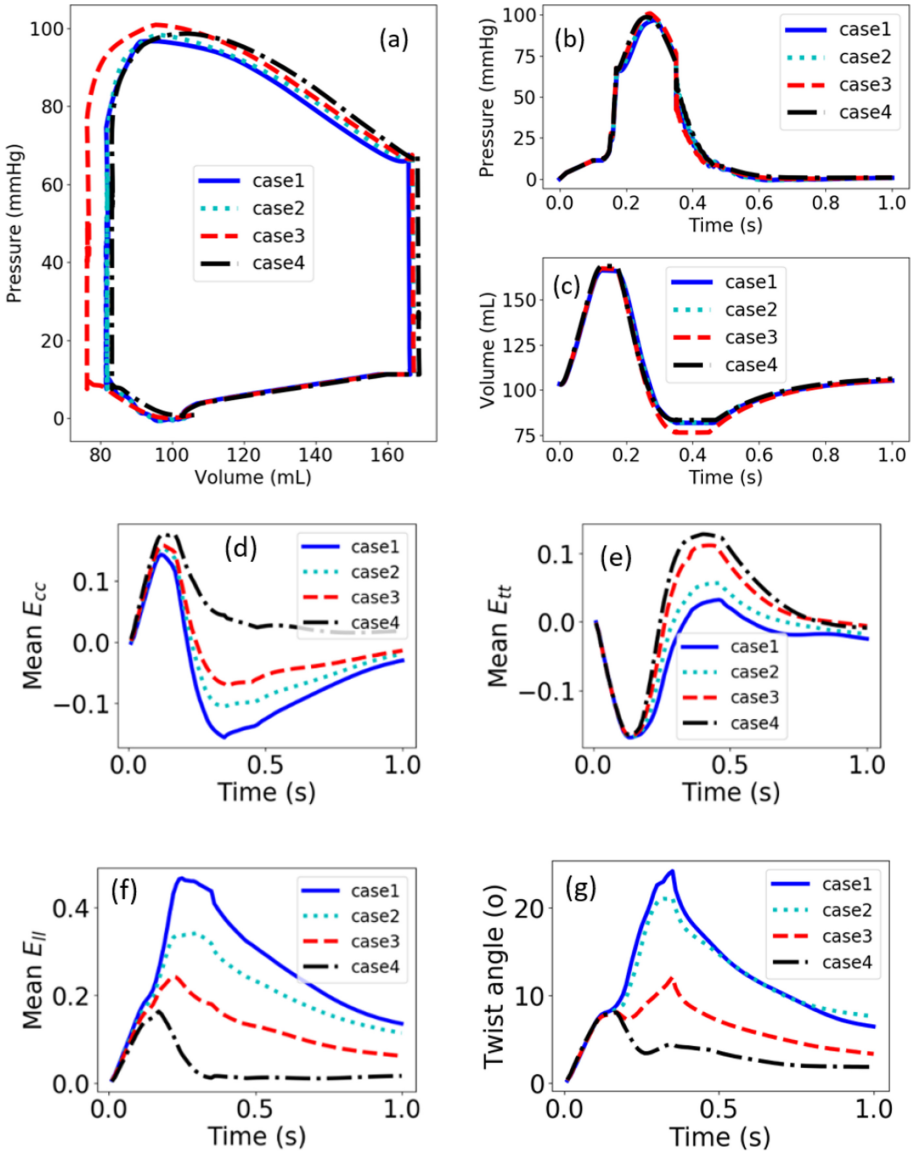

Fig. 4. Effects of the helix angle range on simulated mechanical properties for Cases 1–4: (a) PV loops of LV, (b) left ventricular pressure against time, (c) left ventricular volume against time, (d) mean of all nodal strain in circumferential (E_{cc}), (e) transmural (E_{tt}), (f) longitudinal (E_{ll}) directions, and (g) twist angle of the apex.

As seen in Fig. 4(b)–(c), the ventricles were sequentially inflated subject to a ramping ventricular pressure, activated, contracted and relaxed in the simulation.

In the first inflation phase, the circumferential diameter and longitudinal length of the ventricles were increased, meaning positive circumferential, E_{cc} in Fig. 4(d), and

longitudinal strain, E_{ll} in Fig. 4(f), and the wall thickness was decreased, meaning negative transmural strain, E_{tt} in Fig. 4(e). The longitudinal strain, E_{ll}, was increased during the first 0.1 s due to inflation of the ventricles subject to pressure. Figure 4(f) shows that the longitudinal strain in Case 4 is the lowest. This is because the higher helix angle range than in other cases produces a larger proportion of longitudinally-orientated fibres, providing larger resistance to longitudinal extension than in other cases.

In the systolic phase, the circumferential contraction in Case 1 is the highest, as indicated by the largest negative value of E_{cc} at about t = 0.4 s in Fig. 4(d). The amplitude of circumferential contraction decreases from Cases 1 to 4, as indicated by the increase (less negative values) in E_{cc} at about t = 0.4 s. However, the wall thickening, indicated by E_{tt}, and longitudinal shortening, indicated by the negative values of E_{ll}, increases from Case 1 to 4. The twist angle decreases from Case 1 to 4, indicating that increase in the proportion of circumferentially-orientated fibres (Table 1, fifth column) can lead to increase in ventricular twist.

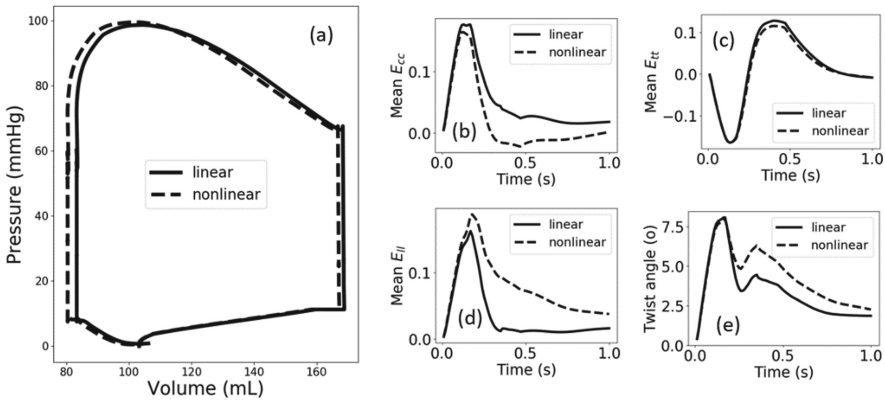

Fig. 5. Effects of linear (Case 4) versus nonlinear (Case 5) transmural gradient in helix angle on simulated mechanical properties: (a) PV loops of LV, (b) mean of all nodal strain in circumferential (E_{cc}), (c) transmural (E_{tt}), and (d) longitudinal (E_{ll}) directions, and (e) apical twist angle.

The effects of linear versus nonlinear transmural variation in helix angle on mechanical function are shown in Fig. 5 through a comparison between Case 4 and Case 5, respectively. The LVEF increases slightly by 2% with nonlinearity in Case 5 versus Case 4 in Fig. 5(a). The mean strain components in Fig. 5 (b)–(e) show that the deformation in diastolic phase before t = 0.2 s is similar, but it is different in the following systolic phase. Figure 5(b) shows that the circumferential strain E_{cc} at around t = 0.4 s is lower in Case 5 than in Case 4, so does the circumferentially expansion. While the effects on the longitudinal strain, E_{ll} in Fig. 5(d), are the opposite. Equivalently, the circumferential contraction in the nonlinear case is larger than in the linear one, while the longitudinal shortening is smaller. The nonlinear transmural variation also increases the circumferential strain rate, indicated by the shorter time over which E_{cc} increases and then decreases for case 5 compared to case 4. However, it decreases the longitudinal strain rate, indicated by the longer time taken for E_{ll} to increase and then decrease see

Fig. 5(d). The twist angle in Fig. 5(e) is larger in the case with nonlinear transmural helical variation than the one with linear.

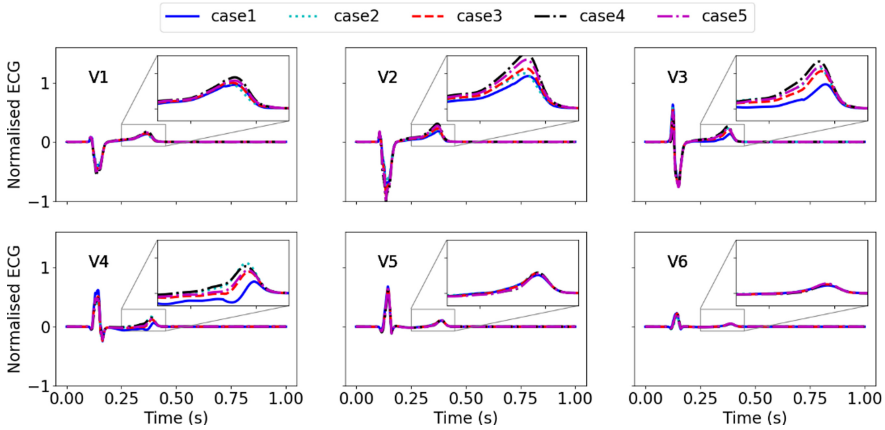

Fig. 6. Comparison of simulated ECG signals in the precordial leads between Cases 1–5 to show the effects of the range and transmural gradient of the helix angle in Table 1. The range increases from 30°~−40° in Case 1 to 90°~−90° in Case 4 with a linear transmural gradient. Case 5 has the same range as Case 4 but with nonlinear transmural gradient, see. The T-waves were zoomed in to show the influence in their amplitudes.

Figure 6 shows the effects of the range and the helix angle transmural gradient on ECGs. In leads V2, V3 and V4, the T-wave onset occurs progressively later from Case 4 to Case 1, which is especially apparent in lead V4. This is consistent with the comparison of repolarisation times between Cases 1 and 4 in Fig. 7, which shows earlier repolarisation of the LV in Case 4 than in Case 1. This could be because there is a greater proportion of longitudinally-oriented fibres in Case 4 than in Case 1, which means the electronic

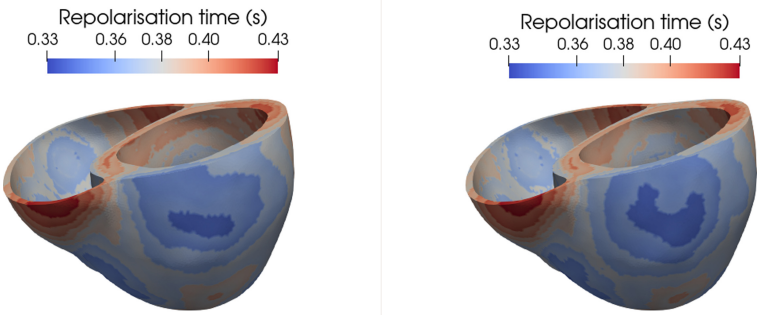

Fig. 7. Repolarisation times map in Case 1 (left) and Case 4 (right). Colour scale shows repolarization time at each ventricular location following propagation from endocardial activation. (Color figure online)

coupling is stronger in the apex-to-base direction, resulting in less heterogeneity in action potential duration and an earlier repolarisation overall.

The other effect is that the T-wave amplitude increases with the helix angle range from Case 1 to 4 in leads V2 to V4 (see Fig. 6). This effect is likely due to differences in the distance between the precordial ECG leads and the systolic deformed ventricles. With increasing transmural fibre angle range, there is decreasing circumferential contraction, thus bringing the anterior portion of the LV in closer proximity to the precordial electrodes, resulting in a larger T-wave amplitude. A similar effect applies to the comparison between Cases 4 and 5, where the introduction of the transmural nonlinearity in Case 5 leads to greater circumferential contraction, resulting in decreased T-wave amplitude.

4 Discussion

In this study, we quantified the effects of the range and transmural gradient of the helix angle, on clinical electrocardiographic and mechanical biomarkers using simulations with a multiscale model of the human biventricular electromechanical function. We found that both electrocardiographic and mechanical biomarkers are influenced by these two helix angle properties, through regulating the proportion of circumferentially-orientated fibres. With an increase in this proportion, the circumferential contraction and twist increase while longitudinal shortening and T-wave amplitude decrease.

The comparison between Cases 1–4 shows that the largest LVEF is achieved in Case 3. This is attributed to the intermediate helix angle range. The lower range leads to an increase in the proportion of circumferentially orientated fibres, see Table 1. Case 1 with the lowest range has the most circumferentially-orientated fibres than other cases, leading to the circumferentially-dominated contraction. While Case 4 with the largest range has the most longitudinally-orientated fibres compared to other cases, leading to the longitudinally-dominated contraction. Case 3 with the intermediate helix angle range could have the optimal composition of circumferential and longitudinal contraction and consequently have the largest LVEF.

The nonlinearity in the transmural variation of the helix angle leads to a slight increase in LVEF of 2%, and also in twist angle (Case 5 versus Case 4 in Fig. 5). This can be explained by the increase in the proportion of circumferentially-orientated fibres as a result of this nonlinearity, see. The positive correlation between the proportion of circumferentially-orientated fibres and twist angle is consistent with analyses of results for Cases 1–4, and further prove that a large proportion of circumferentially orientated fibres plays an important role in ventricular twist. In Fig. 5(e), the twist angle at end of contraction, $t = 0.35$ s, increased by 41% in Case 5 to that in Case 4. The increase in circumferential strain rate and decrease in longitudinal strain rate is also attributed to the increase in the proportion of circumferentially orientated fibres in Case 5.

The results in Fig. 6 showed that the amplitude of T-wave increased with increasing the range of helix angle in Cases 1–4. This was due to a decrease in the proportion of circumferentially-orientated fibres. This correlation is also observed when comparing the ECG of Case 5 to Case 4 in Fig. 6: the amplitude of T-wave was lower in Case 5 than in Case 4. For Case 5, the proportion of circumferentially orientated fibres is larger than for Case 4, see the fifth column of Table 1.

The negative correlation between the proportion of circumferentially-orientated fibres and T-wave amplitude can be explained by the modulation of the distance between deformed ventricles and torso. As seen in the equation for computing the ECG potential or wave amplitude in (1) of [20], a shorter distance between the ventricles and torso will result in a larger amplitude. From Fig. 4(d), Case 4 had the least circumferential contraction or the largest diameters of ventricular cavities, leading to a shorter distance between ventricles and torso, and thus to the location of the ECG leads. Therefore, Case 4 has larger T-wave amplitude than in other cases.

5 Conclusion

A simulation study was conducted using a computational human biventricular model to quantify the effects of the range and transmural gradient of the helix angle on clinical electrocardiographic and mechanical biomarkers, using five models of the helix angle based on *in vivo* DTMRI data of the human heart. We found that both electrocardiographic and mechanical biomarkers are influenced by these two factors, through regulating the proportion of circumferentially-orientated fibres. With an increase in this proportion, the T-wave amplitude slightly decreases, circumferential contraction and twist increase while longitudinal shortening decreases. Thus, an optimal balance between circumferentially and longitudinally oriented fibres is crucial for the effective contraction of the heart. These findings have implications for modelling and simulation studies, and also for potential DTMRI data interpretation and to guide advancements in image acquisition and analysis to characterise human ventricular fibre architecture.

Acknowledgement. This work was funded by a Wellcome Trust Fellowship in Basic Biomedical Sciences to B.R. (214290/Z/18/Z), the CompBioMed2 Centre of Excellence in Computational Biomedicine (European Commission Horizon 2020 research and innovation programme, grant agreements No. 823712). The authors gratefully acknowledge PRACE for awarding access to SuperMUC-NG at Leibniz Supercomputing Centre of the Bavarian Academy of Sciences, Germany through project ref. 2017174226 and Piz Daint at the Swiss National Supercomputing Centre, Switzerland through an ICEI-PRACE project (icp005).

References

1. Hoffman, J.I.E.: Will the real ventricular architecture please stand up? Physiol. Rep. **5**, 1–13 (2017)
2. Sengupta, P.P., et al.: Left ventricular form and function revisited: applied translational science to cardiovascular ultrasound imaging. J. Am. Soc. Echocardiogr. **20**, 539–551 (2007)
3. Levrero-Florencio, F., et al.: Sensitivity analysis of a strongly-coupled human-based electromechanical cardiac model: effect of mechanical parameters on physiologically relevant biomarkers. Comput. Methods Appl. Mech. Eng. **361**, 112762 (2020)
4. Streeter, D.D., Spotnitz, H.M., Patel, D.P., Ross, J., Sonnenblick, E.H.: Fiber orientation in the canine left ventricle during diastole and systole. Circ. Res. **24**, 339–347 (1969)
5. Anderson, R.H., Smerup, M., Sanchez-Quintana, D., Loukas, M., Lunkenheimer, P.P.: The three-dimensional arrangement of the myocytes in the ventricular walls. Clin. Anat. **22**, 64–76 (2009)

6. Greenbaum, R.A., Ho, S.Y., Gibson, D.G., Becker, A.E., Anderson, R.H.: Left ventricular fibre architecture in man. Br. Heart J. **45**, 248–263 (1981)
7. Stoeck, C.T., et al.: Dual-phase cardiac diffusion tensor imaging with strain correction. PLoS ONE **9**, 1–12 (2014)
8. Toussaint, N., Stoeck, C.T., Schaeffter, T., Kozerke, S., Sermesant, M., Batchelor, P.G.: In vivo human cardiac fibre architecture estimation using shape-based diffusion tensor processing. Med. Image Anal. **17**, 1243–1255 (2013)
9. Nielles-Vallespin, S., et al.: In vivo diffusion tensor MRI of the human heart: reproducibility of breath-hold and navigator-based approaches. Magn. Reson. Med. **70**, 454–465 (2013)
10. Tseng, W.Y.I., Reese, T.G., Weisskoff, R.M., Brady, T.J., Wedeen, V.J.: Myocardial fiber shortening in humans: initial results of MR imaging. Radiology **216**, 128–139 (2000)
11. Wang, V.Y., et al.: Image-based investigation of human in vivo myofibre strain. IEEE Trans. Med. Imaging. **35**, 2486–2496 (2016)
12. Carapella, V., et al.: Quantitative study of the effect of tissue microstructure on contraction in a computational model of rat left ventricle. PLoS ONE **9**, 1–12 (2014)
13. Holmes, J.W.: Determinants of left ventricular shape change during filling. J. Biomech. Eng. **126**, 98–103 (2004)
14. Wang, Z.J., et al.: Human biventricular electromechanical simulations on the progression of electrocardiographic and mechanical abnormalities in post-myocardial infarction. EP Europace. **23**, i143–i152 (2021)
15. Tomek, J., et al.: Development, calibration, and validation of a novel human ventricular myocyte model in health, disease, and drug block. Elife **8**, e48890 (2019)
16. Land, S., Park-Holohan, S.-J., Smith, N.P., dos Remedios, C.G., Kentish, J.C., Niederer, S.A.: A model of cardiac contraction based on novel measurements of tension development in human cardiomyocytes. J. Mol. Cell. Cardiol. **106**, 68–83 (2017)
17. Margara, F., et al.: In-silico human electro-mechanical ventricular modelling and simulation for drug-induced pro-arrhythmia and inotropic risk assessment. Prog. Biophys. Mol. Biol. **159**, 58–74 (2020)
18. Holzapfel, G.A., Ogden, R.W.: Constitutive modelling of passive myocardium: a structurally based framework for material characterization. Philos. Trans. R. Soc. A: Math. Phys. Eng. Sci. **367**, 3445–3475 (2009)
19. Santiago, A., et al.: Fully coupled fluid-electro-mechanical model of the human heart for supercomputers. Int. J. Numer. Methods Biomed. Eng. **34**, e3140 (2018)
20. Gima, K., Rudy, Y.: Ionic current basis of electrocardiographic waveforms: a model study. Circ. Res. **90**, 889–896 (2002)
21. Mincholé, A., Zacur, E., Ariga, R., Grau, V., Rodriguez, B.: MRI-based computational torso/biventricular multiscale models to investigate the impact of anatomical variability on the ECG QRS complex. Front. Physiol. **10**, 1103 (2019)